CrossMark

The Colliding Winds of WR 25 in High-resolution X-Rays

Pragati Pradhan[1] , David P. Huenemoerder[1] , Richard Ignace[2] , A. M. T. Pollock[3] , and Joy S. Nichols[4]

[1] Massachusetts Institute of Technology, Kavli Institute for Astrophysics and Space Research, 77 Massachusetts Ave., Cambridge, MA 02139, USA; pragati@mit.edu
[2] Department of Physics & Astronomy, East Tennessee State University, Johnson City, TN 37614, USA
[3] Department of Physics and Astronomy, University of Sheffield, Hounsfield Road, Sheffield S3 7RH, UK
[4] Harvard-Smithsonian Center for Astrophysics, 60 Garden Street, Cambridge, MA 02138, USA

Abstract

WR 25 is a colliding-wind binary star system comprising a very massive O2.5If*/WN6 primary and an O-star secondary in an eccentric orbit with a 208 day period. These hot stars have strong, highly supersonic winds that interact to form a bright X-ray source from wind-collision shocks whose conditions change with stellar separation. Different views through the winds of Wolf–Rayet and O stars are afforded with orbital phase as the stars move about their orbits, allowing for exploration of wind structure in ways not easy or even possible for single stars. We have analyzed an on-axis Chandra/HETGS spectrum of WR 25 obtained shortly before periastron when the X-rays emanating from the system are the brightest. From the on-axis observations, we constrain the line fluxes, centroids, and widths of various emission lines, including He triplets of Si XIII and Mg XI. We have also been able to include several serendipitous off-axis HETG spectra from the archive and study their flux variation with phase. This is the first report on high-resolution spectral studies of WR 25 in X-rays.

Unified Astronomy Thesaurus concepts: Wolf-Rayet stars (1806); Massive stars (732); X-ray astronomy (1810)

1. Colliding Winds of Massive Stars

Massive stars have strong stellar winds, accelerated to high velocities by radiation pressure on millions of UV lines (Castor et al. 1975). Instabilities lead to high-temperature shocks embedded within the wind that are capable of producing detectable X-ray emissions (Lucy & White 1980; Feldmeier et al. 1997). While the X-ray-emitting plasma is thought to be a fairly small fraction of the total wind volume, X-ray spectra provide key diagnostics of this plasma through the emission lines and their profiles: line ratios are sensitive to the luminosity and temperature distribution (Kahn et al. 2001; Waldron & Cassinelli 2007; Walborn et al. 2009), and line profiles are sensitive to the wind structure (Ignace 2001, 2016; Owocki & Cohen 2001; Waldron & Cassinelli 2001; Sundqvist et al. 2012). These individual line-profile studies assume that any specific line is formed by a plasma at the temperature of maximum emissivity of the line. There have also been other *global* approaches to fit the high-resolution X-ray spectrum of a star combining the contributions from multi-temperature plasma components (Hervé et al. 2013). Both the line-by-line and global studies depend on the accurate measurement of high-resolution spectra of these massive stars. Of fundamental interest, for X-ray spectral diagnostics, are the mass loss rate ($\dot{M}$) and the momentum flux ($\dot{M} v_\infty$), with v_∞ the terminal velocity of the wind (e.g., Owocki et al. 2013). Evolutionary models show that large mass loss rates profoundly affect the ultimate state of the star, while the momentum input strongly affects the stellar environment (e.g., Langer 2012; Smith 2014). Their prodigious ionizing UV radiation, of course, also affects their environments to large distances. This feedback can be an important part of galactic evolution.

O stars, which have masses of 15–90 $M_\odot$, typically have terminal velocities of about 2000 km s^{-1} and mass loss rates of the order of $\sim 10^{-6} M_\odot$ yr^{-1} (e.g., Puls et al. 2008). Wolf–Rayet (W-R) stars, which are at a more advanced evolutionary stage, typically having depleted H and enriched C, N, or O, have masses ranging from 10 to 100 $M_\odot$ and terminal velocities of ~ 2000 km s^{-1}, but much larger $\dot{M} \gtrsim 10^{-5} M_\odot$ yr^{-1} (Crowther 2007; Hamann et al.

2019). Some derived fundamental stellar parameters depend critically on model assumptions regarding the degree of clumping in winds, or the law of wind velocity with radius, as examples, which may be difficult to obtain empirically (e.g., Muijres et al. 2011; Sander et al. 2017; Sundqvist et al. 2018; Driessen et al. 2019).

Binary systems provide the opportunity to constrain some of these parameters. For a binary composed of two massive stars, the component winds are expected to collide at supersonic velocities between the stars and generate luminous X-ray-temperature shocks (Prilutskii & Usov 1976; Luo et al. 1990; Stevens et al. 1992; Usov 1992), although this simple expectation does not always prove to be the case (see Rauw & Nazé 2016 for a recent review) for a variety of reasons still under investigation. In the brightest systems, the colliding winds outshine the X-rays from the intrinsic stellar wind by an order of magnitude or more as shown first for the Wolf–Rayet stars by Pollock (1987) including WR 25, whose binary status was only confirmed about 20 yr later. This bright X-ray emission becomes a primary diagnostic of the post-shock plasma (e.g., Pittard & Corcoran 2002; Henley et al. 2003; Pittard & Parkin 2010). The shock position and conditions depend upon the relative momentum flux ($\dot{M} v_\infty$) of each star and the stellar separation (e.g., Cantó et al. 1996; Gayley 2009). In an eccentric system, the stellar separation changes with orbital phase, and we have the opportunity to probe different wind conditions, such as the relative wind velocities at the stagnation point, different orientations of the shocked region, and variations in the stellar radiation fields in the stagnation region. Line-of-sight absorption through cool pre-shock material also occurs, particularly near conjunction phases, and can provide clumping-independent estimates of the mass loss rates (Pittard 2007; Rauw et al. 2014).

For models of colliding-wind interactions, Stevens et al. (1992) presented the basic dynamics of wind shocks with a 2D hydrodynamical analysis. Parkin & Gosset (2011) showed results of 3D hydrodynamical simulations of an eccentric Wolf–Rayet system, including instabilities and generation of

Table 1
Properties of WR 25

Property	Value	Source
Spectral type	O2.5If*/WN6 + O	Crowther & Walborn (2011) Sota et al. (2014)
Minimum masses ($M_\odot$)	75 ± 7, 27 ± 3	Gamen et al. (2008)
Radii ($R_\odot$)	20.24, 13.52	Hamann et al. (2019) Howarth & van Leeuwen (2019)
v_∞ (km s^{-1})	2480, 2250	Hamann et al. (2019) Howarth & van Leeuwen (2019)
log$\dot{M}$ ($M_\odot$ yr^{-1})	-4.6, -5.6	Hamann et al. (2019) Howarth & van Leeuwen (2019)
Period (days)	207.85 ± 0.02	Gamen et al. (2006)
HJD0	$2,451,598 \pm 1$	Gamen et al. (2006)
Eccentricity	0.50	Gamen et al. (2006)
ω (deg)	215 ± 3	Gamen et al. (2006)
$a \sin i$ ($R_\odot$)	156 ± 8	Gamen et al. (2006)
Distance (kpc)	$1.97^{+0.18}_{-0.15}$	Rate & Crowther (2020)

Figure 1. Schematic of the orbit of WR 25, viewed from above the orbital plane, referenced to the position of the W-R-star primary, shown as the blue circle. Relative positions of the O-star secondary are shown as small circles for the on-axis HETG observations in black, and for the serendipitous off-axis observations in gray. Phases for the start of each group of observations are shown near the O-star circles, with days from periastron in parentheses. Orbital parameters are given in Table 1 or references cited there. The arcs represent a cross section of the shock cone, which is nearer to, and concave toward, the O star.
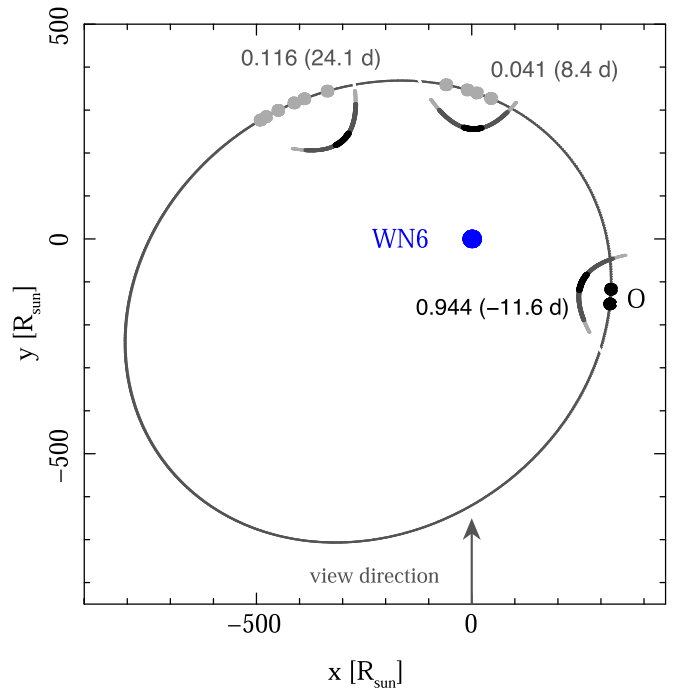
spiral structure in the wind shock cone trailing the secondary. Some classic examples of colliding-wind binaries in eccentric orbits are WR 140, with an 8 yr period (Williams et al. 1990; Pollock et al. 2005; Zhekov 2021), η Car in a 5.5 yr orbit (Hamaguchi et al. 2016; Corcoran et al. 2017), and γ^2 Vel in a 78 day orbit (Skinner et al. 2001; Schild et al. 2004), to name but a few representative studies that demonstrate the importance of orbital phase coverage in X-rays of these types of systems.

In this paper, we will discuss one such colliding-wind binary, WR 25. In Section 2, we review previous X-ray studies of WR 25 along with current estimates for the binary properties. A description of the Chandra observations is presented in Section 3, with results from the high-resolution spectral analysis given in Section 4. Finally, line shapes, ratios, and overall variability of WR 25 are described in Section 5.

2. Characteristics of WR 25

The binary system WR 25 (HD 93162), whose properties are noted in Table 1, comprises an O2.5If*/WN6 (Crowther & Walborn 2011) primary of minimum mass $M_1 = 75 \pm 7\,M_\odot$ with an O-star secondary of minimum mass $M_2 = 27 \pm 3\,M_\odot$ (Gamen et al. 2008) in an orbit with a 208 day period and an eccentricity of about $e = 0.50$ with an uncertainty of perhaps 0.10 (Gamen et al. 2006). Apart from its minimum mass, little is known about the otherwise unclassified O-star secondary, although the mass does suggest that the well-studied O4If star ζ Pup (Howarth & van Leeuwen 2019) is a suitable analog for suggesting the plausible set of secondary properties shown in Table 1.

The primary is a contender for the most massive star in the Milky Way, a status it shares with other stars of similar spectral type, i.e., hydrogen-rich WN stars in binary systems, including WR 20a, WN6ha+WN6ha (Rauw et al. 2004), WR 21a, O3/ WN5ha+O3Vz((f*)) (Tramper et al. 2016), and WR 22, WN7h +O9III-V (Schweickhardt et al. 1999), also all in Carina; and WR 43a, WN6ha+WN6ha (Schnurr et al. 2008) in the starburst-analog cluster NGC 3603. Their binary periods range from a few days to several months. A similar set of perhaps even more

extreme stars is to be found in the lower-metallicity LMC including Melnick 34 (Brey 84), which the Chandra T-ReX survey revealed as a 155 day period WN5h+WN5h binary of the highest X-ray luminosity ($>10^{35}$ erg s^{-1}) of any colliding-wind binary including η Carinae (Pollock et al. 2018) and the most massive known binary system with components of 139 $M_\odot$ and 127 $M_\odot$ (Tehrani et al. 2019). Evolutionary spectroscopic analysis shows that these stars are all very young, very massive W-R stars still burning hydrogen on the main sequence, in contrast to the more evolved classic WN and WC stars of lower mass, in which hydrogen is usually absent.

WR 25 is the nearest and X-ray-brightest of this important class of very massive stars. It lies in the Carina region at a Gaia DR2 distance of 1.97 kpc and has figured prominently in studies of massive stars since the beginning of hot-star X-ray astronomy and the report of its discovery in the first-light issue of the Einstein Observatory (Seward et al. 1979). It is one of the very few colliding-wind binary systems with complete orbital coverage. This has been procured through 266 separate Swift observations, mostly granted to one of us through 13 separate Target-of-Opportunity requests for WR 25 under Target ID 31097 between 2007 and 2018, which have been complemented with occasional more precise XMM-Newton, Suzaku, and NuSTAR measurements, often available serendipitously through observations of its neighbor η Carinae. The X-ray light curve shows the distinct X-ray brightening expected from colliding winds moving toward periastron (Pollock 2012; Pandey et al. 2014; Arora et al. 2019). In Figure 1 we show the orbital geometry and in Figure 2 details of the notably asymmetric phased light curve from Swift. The soft-to-hard
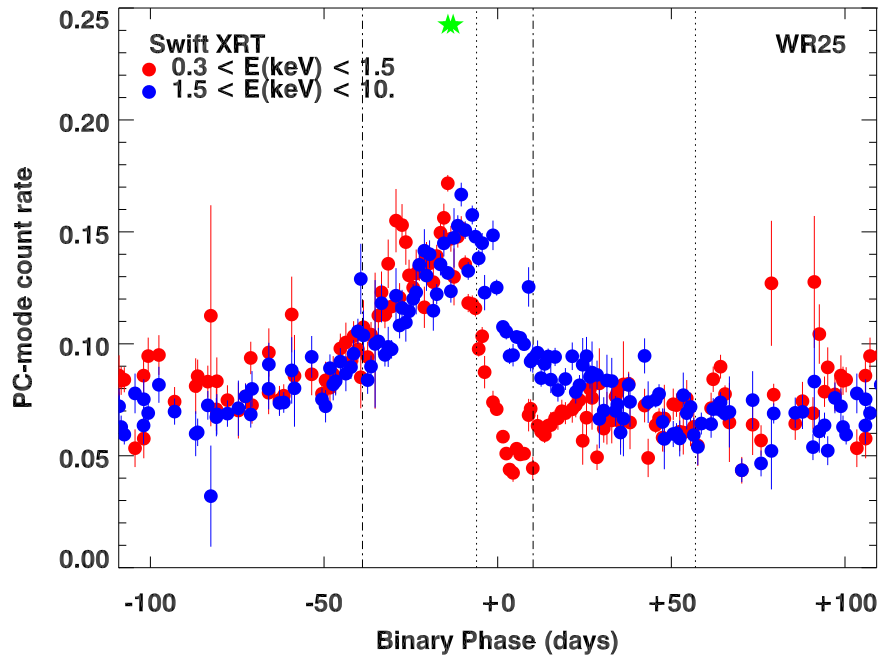
Figure 2. The Swift XRT light curve of WR 25 in two bands. The soft band (0.3–1.5 keV) is shown in red, and the hard band (1.5–10 keV) in blue. From the optical radial-velocity orbital solution, the vertical dotted lines mark quadratures (extrema in radial velocity), while the dotted–dashed vertical lines denote conjunctions, with the O star in front about 40 days before periastron, and the W-R star in front about 10 days after, where phase 0.0 days is periastron. Two overlapping green stars mark the phases of the pointed Chandra/HETGS observations at maximum light near quadrature corresponding to the black circles in Figure 1. The ephemeris used is given in Table 1.

flux ratio is constant throughout most of the orbit but starts to decrease about 10 days before periastron as the W-R primary moves in front, reaching a well-defined minimum about 2 days before the conjunction predicted by the optical radial-velocity solution, which might not precisely track the primary's orbital motion (Grant et al. 2020) but may also suggest a slightly higher orbital eccentricity.

From the mass loss rates and terminal velocities in Table 1 the stagnation point of the colliding flows is expected to be closer to the O star, and thus the shock cone convex toward the W-R star. Analysis by Arora et al. (2019) suggested that the wind velocity of each star at the stagnation point changes significantly over the course of the orbit, from about $1600 \, \mathrm{km \, s^{-1}}$ at periastron to $2200 \, \mathrm{km \, s^{-1}}$ at apastron, although this does not coincide with any obvious softening of the spectrum (Pollock & Corcoran 2006). The shock may transition from adiabatic to radiative near periastron, and perhaps even undergo radiative braking (Gayley et al. 1997) through proximity to the intense O-star radiation field. The change in the pre-shock relative velocity of wind–wind collision from about $3200 \, \mathrm{km \, s^{-1}}$ to $4400 \, \mathrm{km \, s^{-1}}$ should result in a corresponding change in the post-shock temperature of more than 50%.

3. Observations

To better quantify the plasma conditions, we have obtained Chandra/HETG high-resolution X-ray spectra slightly before periastron (black circles in Figure 1, green stars in Figure 2), at phases in 2016 August when the Swift rates predicted a maximum. With these observations we can potentially determine line centroids, resolve lines widths, determine plasma temperatures from line strengths and the continuum shape, and constrain X-ray source locations from the photoexcitation in He-like ions' forbidden-to-intercombination line ratios. From line-to-continuum

ratios, we can explore possibilities of unusual abundances or collisionless plasma effects.

Although quite far off-axis ($\sim 10'.5$), we have also analyzed several serendipitous Chandra/HETG spectra of WR 25 taken more than 10 yr earlier during high-resolution observations of other hot stars in Carina. The instrumental profile at the source locations, however, is too broad to characterize line widths or centroids accurately. The off-axis data provide some line and broadband fluxes, useful for study of the stellar wind and the structure of the wind-shock region through variations with phase.

Table 2 provides a log of the observations, the exposure, and the orbital phases, for both the on-axis and off-axis pointings.

4. High-resolution Spectral Analysis

4.1. On-axis Observations

The counts spectra for the observations were extracted using `TGCat` reprocessing scripts (Huenemoerder et al. 2011), using CIAO (Fruscione et al. 2006) version 4.8 and Calibration Database version 4.7.2. Since the two on-axis observations are taken less than a day apart with orbital phases that differ by only 0.007 (see table 2), we combined the negative and positive first-order spectra from both the observations to get one combined spectrum each for HEG and MEG. The advantage of doing this is to increase the signal-to-noise ratio, facilitating high-resolution spectral analysis and also reducing the number of model bins, thereby reducing execution time in model evaluation during fitting.

We fit the spectra both with a global plasma model and line-by-line. The global model gives a broad characterization of plasma conditions, within the parameters of the model, under the assumption that all the lines have the same shape and Doppler offset. The line-by-line fits relax the latter assumptions, and are

Table 2
Observations Analyzed in the Current Work with Time of Observation,
Observation Identifier, Exposure, Orbital Phase Including Days from
Periastron, and Relative Stellar Separation

Start Time	ObsID	Exposure (ks)	ϕ	ΔT (days)	$R/R_{\max}$
(on-axis pointings)					
2016-08-10T15:19:33	18616	28	0.944	−11.6	0.403
2016-08-11T23:28:52	19687	57	0.951	−10.2	0.388
(serendipitous off-axis pointings)					
2005-11-08T07:19:58	7201	18	0.041	8.4	0.373
2005-11-09T14:44:53	7204	33	0.047	9.7	0.385
2005-11-10T11:02:37	7202	10	0.051	10.6	0.392
2005-11-12T07:41:15	7203	27	0.060	12.4	0.411
2005-11-29T22:35:38	5397	10	0.145	30.1	0.611
2005-12-01T12:19:53	7228	20	0.152	31.6	0.627
2005-12-02T08:44:16	7229	20	0.156	32.5	0.636
2006-06-19T18:00:43	7341	53	0.116	24.1	0.544
2006-06-22T10:18:52	7342	49	0.129	26.7	0.575
2006-06-23T17:45:18	7189	18	0.135	28.0	0.589

independent of any global plasma model since they are local parametric functional fits.

All spectral fitting was performed using the Interactive Spectral Interpretation System (ISIS software,[5] Houck & Denicola 2000), which also provides interfaces to AtomDB (Smith et al. 2001; Foster et al. 2012) as well as to xspec (Arnaud 1996) models.

For global spectral modeling, we fit the 1.5–20 Å spectrum of WR 25 with a plasma model which uses a power-law emission measure distribution, as described in detail by Huenemoerder et al. (2020). The model is of the form $d\mathrm{EM}/dT = n_e n_H \, dV/dT \propto (T/T_{\max})^{-\beta}$, where $d\mathrm{EM}/dT$ is the differential emission measure, V is the volume of X-ray-emitting plasma, n_e and n_H are the electron and hydrogen number densities, respectively, T is the plasma temperature, which we limit to a range from $T_{\min}$ to $T_{\max}$, and the exponent on temperature is β. This model is obtained from line and continuum emissivities from the Astrophysical Plasma Emission Code (APEC) as stored in the atomic database, AtomDB. We used the abundances from Asplund et al. (2009). WR 25 likely has a reduced abundance of hydrogen and increased helium in the WN component. Hence interpretation of the normalization and relative abundances requires caution; Ignace et al. (2000) and Schulz et al. (2019) provide a method for scaling of parameters in low-hydrogen plasmas. AtomDB's collisional ionization equilibrium (CIE) emissivities do not include effects of high density or UV photoexcitation of the He-like forbidden (f) and intercombination (i) lines. As we show later in Section 5.2, we do not have evidence that the f/i ratio is altered from its CIE value. Hence, we have included the Si XIII, Mg XI, and Ne IX regions in our fits. The model also assumes that all emission lines have the same Gaussian shape and Doppler shift, and that neutral absorption is all in the foreground. As such, the model represents the mean characteristics of the emitting plasma and is not a detailed dynamical and geometrical model. Uncertainties on model parameters were determined from a Markov Chain Monte Carlo evaluation (an ISIS implementation, "emcee", of the Python code of

Foreman-Mackey et al. 2013) to search parameter space and form confidence contours.[6]

The data, fitted model, and residuals are shown in the top panel of Figure 3. The spectrum of WR 25 has many strong emission lines, primarily of H- and He-like ions, but also of many Fe ions. Below about 10 Å, the underlying continuum is also prominent. Model parameters are given in Table 3.

Parametric line fitting was performed using the plasma model as a guide to line identification and probable blend assessment. Emission lines were fitted in groups of overlapping or close features, using sums of Gaussian profiles folded through the instrument response. If a feature was too blended or too weak for an unconstrained fit, it was restricted accordingly, either by constraining its parameters to a stronger line's parameters or by freezing the position or width and fitting the flux. For example, for the weak Fe XXV line, we froze the wavelength to the theoretical value and the Gaussian σ to the best-fit value to constrain only the flux. Since the r and i lines of Ar XVII cannot be resolved with HETG, both lines were fitted with a single Gaussian while the f line was tied in wavelength offset and Gaussian σ to the $(r + i)$ line's value. The S XV and Si XIII triplets were fitted with three Gaussians with the wavelength offsets and Gaussian σ of the i and f lines tied to the r line. Being blended with Ne X, the Mg XI region was fitted with six Gaussians with the wavelength offset and Gaussian σ of five lines fixed to the strongest Mg XI r line. We also froze the Gaussian σ of the Ne X β and Ne X γ lines since this region is heavily blended with Fe, making independent constraints difficult. The Gaussian σ and wavelength offsets of Fe XVII and Fe XXI were tied to the main Ne X α line. The Ne IX region was fitted with five lines with the wavelength offset and Gaussian σ of four lines tied to the strongest Ne IX r line. All the isolated H lines (S XVI, Mg XII, Ne X, O VIII) were freely fitted. Results of emission line fits are given in Table 4; for tied parameters in constrained fits, uncertainties have null values. The regions fit are shown in Figures A.1–A.4 in the Appendix.

The plasma model also served to provide a continuum model, since in crowded regions, with wind broadening, the local minima are not good approximations to the continuum. We also examined the line profiles of strong lines in detail, considering whether a Gaussian shape is adequate, and we studied in detail the He-like ratios for evidence of photoexcitation in the forbidden-to-intercombination line ratio. Results will be discussed in subsequent sections. Note that we did not include neutral absorption in these line fit models, hence the flux is as observed at Earth.
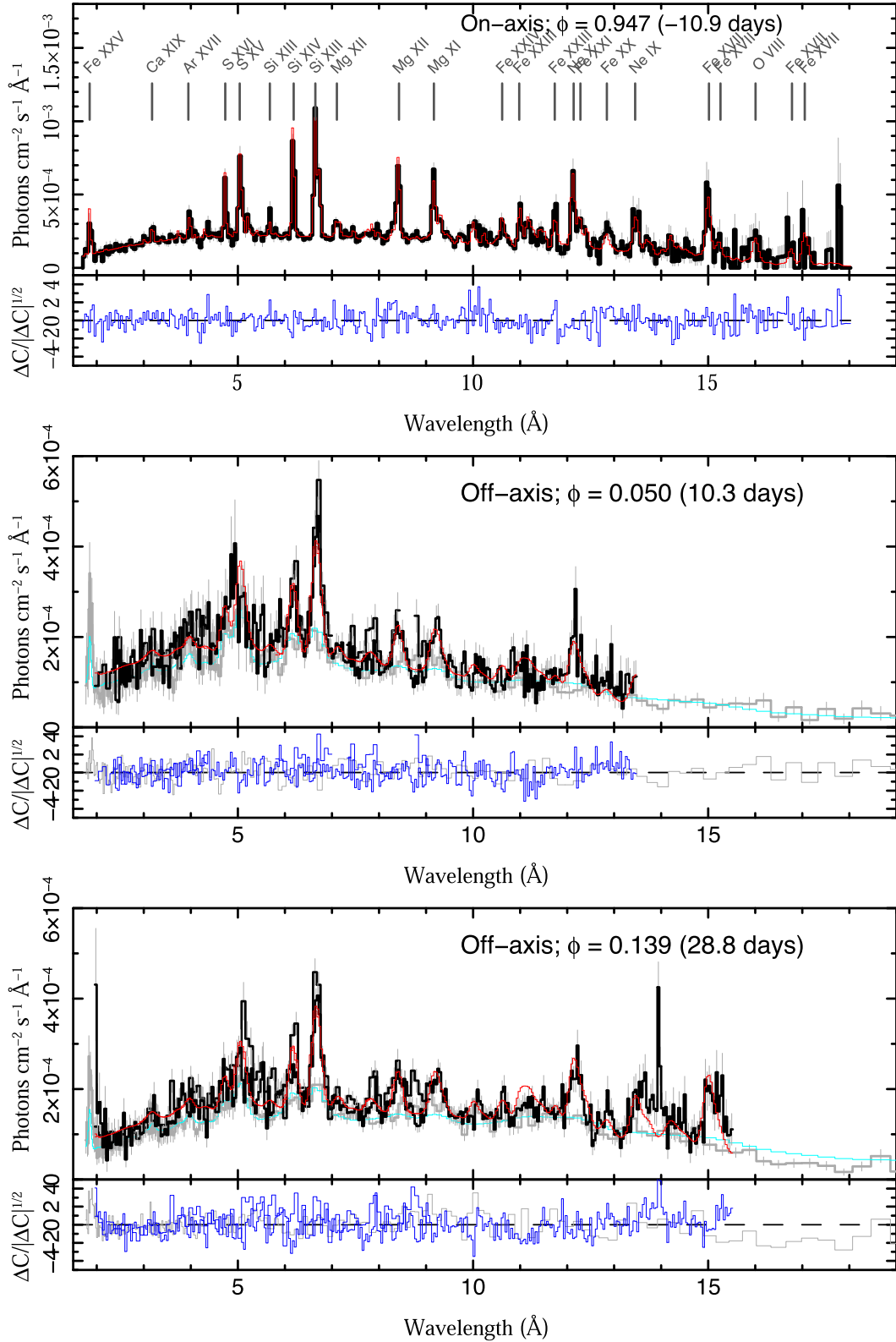
4.2. Serendipitous Off-axis Observations

We analyzed 10 off-axis serendipitous observations of WR 25 (gray circles in Figure 1 at phases ∼0.05 and ∼0.14). These were taken with the source at about 10 arcmin off-axis, which significantly blurs the spectrum due to the large point-spread function. The spatially broad spectra (in the cross-dispersion direction) were also truncated obliquely in some orders by the detector boundary, making the calibration uncertain. Hence we ignored wavelengths beyond about 14 Å. The shortest wavelengths, below about 2 Å, were also compromised by overlap of the wide HEG and MEG spectral arms, precluding extraction of Fe XXV.

---

[5] https://space.mit.edu/cxc/ISIS/index.html

[6] The ISIS version is described at https://www.sternwarte.uni-erlangen.de/wiki/index.php/Emcee and is available as part of the isisscripts package available at https://www.sternwarte.uni-erlangen.de/isis/.

Figure 3. Top: pointed Chandra/HETGS flux spectrum of WR 25 (black), fit with a plasma model which uses a power-law emission measure distribution (red) and residuals (blue, lower panel). Center and bottom plots show the serendipitous off-axis HETGS spectra with their fitted high-resolution models convolved with a Gaussian appropriate for the off-axis blurring. The gray curve (with error bars) is the zeroth-order spectrum, and its corresponding model is the light solid line. The numbers in parentheses give the days from periastron.

For the zeroth-order spectra, we performed analysis only for the off-axis observations, since the on-axis spectra were heavily piled up. We downloaded the relevant ObsIDs from TGCat (Huenemoerder et al. 2011) and used dmextract to extract the source spectrum by selecting circular regions of 60″ centered on the source position. The relevant response files and

Table 3
Parameters of the Emission Measure Model

Parameter	Value $\phi = 0.95$	σ	Value $\phi = 0.05$	σ	Value $\phi = 0.13$	σ	Units
$norm$	0.032	0.003	0.025	0.003	0.024	0.002	cm^{-5}
β	1.02	0.08	1.22	0.09	1.18	0.07	
$\log T_{\max}$	7.70	0.03	7.93	0.04	7.82	0.03	dex K
$\log T_{\min}$	6.00	⋯	6.00	⋯	6.00	⋯	dex K
FWHM	2232	70	1338	⋯	1338	⋯	km s^{-1}
v_{Doppler}	−303	32	−303	⋯	−303	⋯	km s^{-1}
A(Ne)	0.60	0.09	0.48	0.11	0.42	0.05	
A(Mg)	0.64	0.04	0.51	0.06	0.41	0.04	
A(Si)	0.85	0.05	1.02	0.08	0.81	0.05	
A(S)	1.10	0.10	1.73	0.20	1.20	0.10	
A(Fe)	0.48	0.05	0.37	0.06	0.56	0.03	
N_{H}	0.65	0.04	0.74	0.05	0.56	0.03	10^{22} cm^{-2}
f_x(obs)	1.04×10^{-11}		7.80×10^{-12}		7.69×10^{-12}		erg cm^{-2} s^{-1}
$f_x(N_{\mathrm{H,ISM}})$	1.42×10^{-11}		1.09×10^{-11}		9.55×10^{-12}		erg cm^{-2} s^{-1}
$f_x(N_{\mathrm{H}} = 0)$	3.91×10^{-11}		2.98×10^{-11}		2.72×10^{-11}		erg cm^{-2} s^{-1}

Note. The normalization is related to the emission measure via $norm = [10^{-14}/(4\pi d^2)]\int n_e n_{\mathrm{H}}\, dV$, subject to reinterpretation for H-deficient, He-rich plasmas as stated in the text. The broadening, given by the FWHM, was treated as a Gaussian line profile with the same velocity for all lines. Abundances, $A(Z)$, are scale factors on the number fractions relative to hydrogen of Asplund et al. (2009) (and were 1.0 if not listed). Uncertainties (σ) are given as 68% confidence error bars, as determined with Markov Chain Monte Carlo methods; if the parameter was frozen, then the uncertainty is given as "⋯". For the off-axis data ($\phi = 0.05, 0.13$), unspecified parameters were taken from the on-axis fits and frozen. Fluxes were evaluated from the fitted model over the band 1.0–40 Å (0.3–12 keV). Pandey et al. (2014) estimated the nonlocal column pf the interstellar medium (ISM) to be about 0.37×10^{22} cm^{-2}; the line for $f_x(N_{\mathrm{H,ISM}})$ is flux-corrected for only this amount.

the ancillary files were generated with `mkacisrmf` and `mkarf`. We corrected the ancillary files for the aperture efficiency factor using `arfcorr` as recommended in the CIAO website.[7]

To fit the HEG/MEG spectra, we determined the blur scale from the zeroth-order extent, then used a Gaussian convolution model (Xspec's "`gsmooth`") on our APEC-based power-law emission measure model. Since the wavelength range of the dispersed off-axis spectrum is somewhat limited, we also simultaneously fit the zeroth-order spectra. Given the off-axis blurring of the image, CCD pile-up was not an issue, as it is for the on-axis zeroth order. To account for possible systematic differences in the calibrations of zeroth order and dispersed effective area, we introduced a free renormalization parameter on the zeroth order, whose value was 0.80 ± 0.01, which is somewhat larger than the nominal 5% expected calibration uncertainty. We fit this model to spectra in two phase groups (freezing the broadening and Doppler shift to the high-resolution fit values). Uncertainties were determined via `emcee`. The results are shown in Figure 3 and fitted parameters are listed in Table 3.

5. Discussion

In a colliding-wind binary, when the component stars are closest to each other at periastron, the shocked-wind region far outshines the X-ray emission from the components' stellar winds in isolation. The components of the WR 25 system are similar to ζ Pup and WR 6, which have luminosities of about 2×10^{32} erg s^{-1} (Nazé et al. 2012) (using a distance of 332 pc from Howarth & van Leeuwen 2019) and 8×10^{32} erg s^{-1} (Huenemoerder et al. 2015), respectively. If we assume the interstellar line-of-sight column density to WR 25 of 3.7×10^{21} cm^{-2} estimated by Pandey et al. (2014), then the luminosity implied by the spectrum at $\phi = 0.96$ is

about 9×10^{33} erg s^{-1}, nearly an order of magnitude larger than that expected from the individual stellar winds in isolation. The changing distance between the components around an eccentric orbit causes the wind–wind collision to occur at different velocities in the accelerating matter, and the varying aspect lets us view the shock from different angles, as well as through different wind columns of the two stars. Using high-resolution spectroscopy, we can therefore study the temperature and dynamics of the shock through line fluxes and profiles. The broadband spectral shape is also sensitive to temperature and the line-of-sight neutral absorption.

There has been significant progress in understanding the high resolution of colliding-wind binary systems using observations from Chandra and XMM-Newton. From the HETG observations of γ^2 Vel (WC8 + O7.5), it was possible to characterize the plasma temperatures and identify the radius of emission of He-like triplets. The He-like triplets showed strong forbidden lines with no significant weakening from collision or photoexcitation, which implied that some lines such as Ne IX triplet were formed in the cooler plasma components at tens of stellar radii from the O star (Skinner et al. 2001). Such a presence of strong forbidden line emission has also been seen in other colliding-wind binaries such as η Carinae, WR 147, WR 140, and WR 48a (Corcoran et al. 2001; Pollock et al. 2005; Zhekov & Park 2010; Zhekov et al. 2014), and is in sharp contrast to the findings of other isolated stars such as ζ Pup, for example (Huenemoerder et al. 2020). Significant Doppler shifts in the pre-periastron phase of WR 140 indicated that during this phase the bow shock approaches the line of sight, and no such Doppler shifts were seen when the bow shock aligned perpendicular to the line of sight (Pollock et al. 2005). On the other hand, detection of Doppler shift in θ Muscae when seen in the context of the geometry of the system indicated that this is possibly a triplet system (Sugawara et al. 2008).

Table 4
Emission Line Parameters for the On-axis Observations

Line	λ_0	Δv	$\sigma_{\Delta v}$	f_x (10^{-5} phot-ons	σ_f	FWHM	σ_{FW}
	(Å)	(km s^{-1})		cm^{-2} s^{-1})		(km s^{-1})	
Fe XXV (r)	1.858	⋯	⋯	1.64	0.38	⋯	⋯
Ar XVII (r+i)	3.949	−56	238	0.69	0.18	1595	497
Ar XVII (f)	3.994	⋯	⋯	0.62	0.17	⋯	⋯
S XVI α	4.730	162	215	2.55	0.35	2915	476
S XV (r)	5.039	−278	310	2.62	0.68	2453	446
S XV (i)	5.065	⋯	⋯	0.84	0.61	⋯	⋯
S xv (f)	5.102	⋯	⋯	1.44	0.34	⋯	⋯
Si XIII β	5.681	−266	326	1.18	0.28	2575	731
Si XIV α	6.183	−263	65	4.83	0.26	2339	149
Si XIII (r)	6.648	−242	67	5.49	0.37	2303	135
Si XIII (i)	6.687	⋯	⋯	0.96	0.33	⋯	⋯
Si XIII (f)	6.740	⋯	⋯	2.97	0.23	⋯	⋯
Mg XII α	8.422	−332	80	3.73	0.31	2160	198
Mg XI (r)	9.169	−291	133	3.20	0.37	1985	275
Mg XI (i)	9.230	⋯	⋯	0.57	0.36	⋯	⋯
Ne x ζ	9.291	⋯	⋯	0.52	0.51	⋯	⋯
Mg XI (f)	9.314	⋯	⋯	0.47	0.52	⋯	⋯
Ne x ϵ	9.362	⋯	⋯	0.38	0.29	⋯	⋯
Ne x δ	9.481	⋯	⋯	0.20	0.21	⋯	⋯
Ne x γ	9.708	⋯	⋯	0.26	0.20	⋯	⋯
Ne x β	10.239	⋯	⋯	⋯	⋯	⋯	⋯
Ne X α	12.135	−387	128	6.33	0.59	2568	292
Fe XVII	12.266	⋯	⋯	2.74	0.47	⋯	⋯
Fe XXI	12.390	⋯	⋯	2.78	0.48	⋯	⋯
Ne IX (r)	13.447	−526	147	2.99	0.68	1695	246
Fe XIX	13.497	⋯	⋯	0.11	0.48	⋯	⋯
Ne IX (i)	13.552	⋯	⋯	2.77	0.70	⋯	⋯
Ne IX (f)	13.699	⋯	⋯	1.69	0.51	⋯	⋯
Fe XVII	13.825	⋯	⋯	0.94	0.45	⋯	⋯
Fe XVII	15.014	−477	183	5.77	1.10	2466	498
Fe XVII	15.261	⋯	⋯	1.02	0.52	⋯	⋯
O XVIII β	16.006	−561	184	3.56	1.24	3441	1781
Fe XVII	17.051	−527	109	2.04	1.14	1529	1078
Fe XVII	17.096	⋯	⋯	1.24	0.87	⋯	⋯

Note. λ_0 is the theoretical wavelength; for each line, the velocity, error on velocity, flux, error on flux, FWHM, and error on FWHM are denoted by Δv, $\sigma_{\Delta v}, f_x, \sigma_f$, FWHM, and σ_{FW} respectively. Fluxes are only reported for the lines where Gaussian width was frozen and where the wavelength was tied to their relative offsets from the resonance line (see Section 4.1). For these lines, Δv, $\sigma_{\Delta v}$, FWHM, and σ_{FW} are not present since the wavelength offsets or Gaussian width were tied to a main line, and we denote this by "⋯". All errors are calculated for 1σ confidence level limits.

Given such a variation in emission line properties at different orbital phases, we would ideally like to monitor the emission lines around the orbit. Hence, with only high-resolution spectra at just before periastron for WR 25, this study represents only a start at a detailed view of WR 25 in high-resolution X-rays.

From the local line fits to the on-axis observations near $\phi = 0.94$ (see Table 4 and Figures A.1–A.4), we find that there is a general blueshift of the centroid from the rest wavelength by about $-300 \, \mathrm{km \, s^{-1}}$, with a possible decreasing trend in centroid with increasing wavelength. In Figure 4, the points with error bars show these line-fit results. We also explored another approach, using the global plasma model as a starting point, and refit only the normalization, Doppler shift, and broadening in several wavelength regions. The global model, in contrast, used a common offset and broadening for all lines.
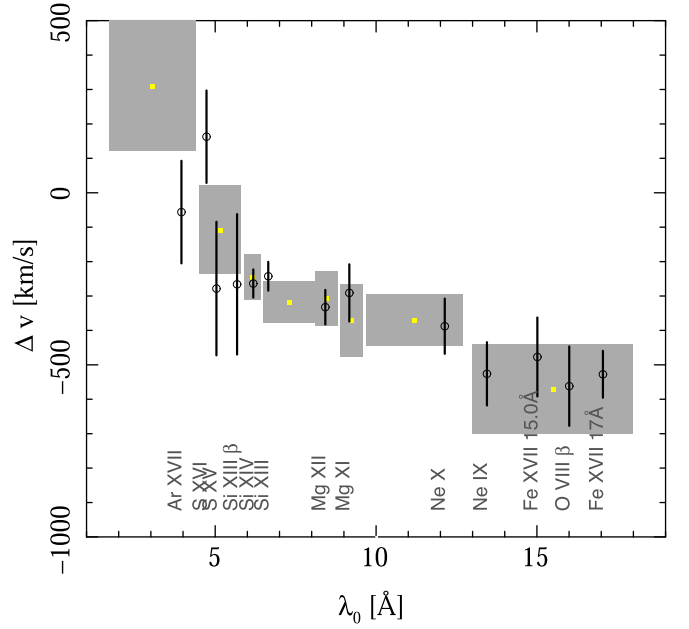

Figure 4. The line centroid velocity offsets from rest wavelengths are shown for two different approaches. The black circles with error bars show the values from the Gaussian fits to line groups. The gray shaded rectangles show the result of piecewise plasma model fits for the Doppler shift and broadening in several wavelength regions. Error bars and the vertical extent of gray shading indicate uncertainties of one standard deviation, while the widths of the gray rectangles indicate the wavelength region fit.

This is of course not independent of the Gaussian line fitting, but takes advantage of the multiplexing of many features in the region, and the underlying plasma model implicitly handles line blends. The result is shown as the shaded regions in Figure 4, and the trend with wavelength is very clear.

Since we are viewing the wind–wind collision shock cone nearly edge on (perpendicularly to the line between stellar centers), we should expect broad lines with an apparent blueshift if the receding material is obscured by foreground absorption by the shock-cone flow or neutral plasma in the stellar wind. In Figure 5, we can see that the lines are broad and seem independent of wavelength. Further investigation shows that a linear fit to the Δv data is not consistent with a constant value, within the uncertainties, and the trend of decreasing Δv with increasing wavelength is likely real. Similarly, a linear fit to the Δv fit values from the plasma model (white dots centered in gray boxes) indicates that a constant value is not consistent with the model fits. However, linear fits to the FWHM data, as well as the FWHM fit values of the plasma model, are consistent with a slope of 0, based on errors in the slope, so we do not suggest a trend of FWHM with wavelength.

The ratio of wind momenta, $\eta = (\dot{M}_s v_{\infty,s})/(\dot{M}_p v_{\infty,p})$, is in the range from 0.2 to 0.5, given the parameters in Arora et al. (2019). For these values, Pittard & Dawson (2018) find opening angles of the primary (W-R star) shock to be roughly $60°–90°$ (from the secondary to the stagnation point to the contact discontinuity line or primary shock envelope). At $\phi = 0.94$ we should have a significant amount of plasma moving parallel to the line of sight (e.g., Henley et al. 2003), and indeed we do see broad profiles, comparable to the primary's wind velocity (Figure 5). Determining whether this is indeed due to the flow in the shock cone will require spectra at phases near conjunctions, when such a flow would be
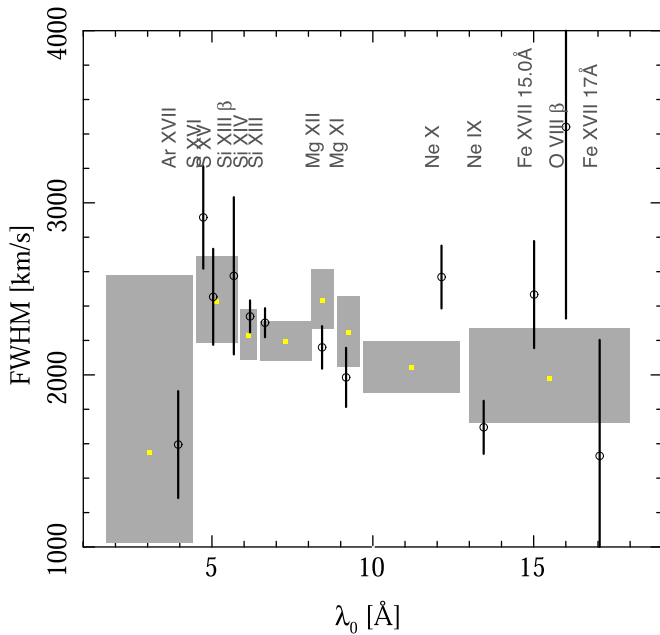
Figure 5. The line widths are shown from the Gaussian fits to line groups as points with error bars, and from piecewise plasma model fits, as in Figure 4.

transverse to the line of sight, and line widths would be smaller and have different velocity offsets.

Our plasma model assumes a power-law emission measure distribution. There is some theoretical justification for this form for stellar winds (Cassinelli et al. 2008; Krtička et al. 2009; Ignace et al. 2012). How well a power-law representation applies in colliding winds is an open question, though it does provide a reasonably good fit to the spectrum, as seen in Figure 3. The model has a parameter specifying a high-temperature cutoff. The continuum comes from thermal bremsstrahlung and bound–free processes, and each has an exponential cutoff at short wavelengths. Furthermore, the region below about 10 Å has a strong continuum and relatively sparse emission lines from high-temperature ions, and is least affected by line-of-sight neutral plasma absorption. Hence, the high-temperature cutoff should be a fairly robust indicator of the maximum pre-shock velocities, under the assumption of strong shocks and emissivities in collisional ionization equilibrium. Using the maximum temperature of 50 MK (see Table 3), a mean molecular weight μ for a highly ionized plasma of 0.7 appropriate for an He-enriched plasma (for comparison, abundances of Asplund et al. 2009 imply $\mu \sim 0.6$), and the relation for a strong shock, $kT = \frac{3}{16}\mu m_H v^2$, in which T is the post-shock temperature, v is the pre-shock velocity, and k is Boltzmann's constant, we find a maximum relative shock velocity $v \approx 1918$ km s^{-1} (with a formal statistical uncertainty of 66 km s^{-1}). Arora et al. (2019) estimated that at $\phi = 0.9$ each wind has a velocity of about 1800 km s^{-1} at the collision, so we might expect anything up to 3600 km s^{-1}. Given that the emergent spectrum is from a larger region where plasma is cooling, our estimate is a plausible value.

5.1. Line Shapes

Our models, plasma or line groups, have so far assumed Gaussian profiles. There is no a priori reason for the emission lines being Gaussian. The instrument response is highly

Gaussian, but these are resolved features, with an FWHM of several resolution elements. Henley et al. (2003) have shown how colliding-wind regions could produce a wide variety of profiles, from narrow and single-peaked, to broad and double-peaked, suggesting a careful review of the observed line shapes.

The best, relatively isolated and strong feature in the WR 25 spectrum is that of the H-like Mg XII. This is an unresolved doublet with emissivities in a 2:1 ratio: 8.4192 Å and 8.4246 Å, so the flux-weighted wavelength is 8.4210 Å. The only significant nearby feature, according to the plasma model, is Fe XXIII 8.3038 Å, with a flux at least 15 times smaller. To investigate whether lines are asymmetric, we fit the Mg XII region profiles with a Weibull distribution, whose shape can range from exponential, to Gaussian-like, to asymmetric with a tail on either the high or low side of the maximum:

$$f(\lambda; q, \sigma, \lambda_0) = \frac{q}{\sigma}\left(\frac{\lambda - \lambda_0}{\sigma}\right)^{q-1} \exp\left[-\left(\frac{\lambda - \lambda_0}{\sigma}\right)^q\right] \quad (1)$$

in which $q > 0$ is a shape parameter, $\sigma > 0$ is the scale, and λ_0 is an offset. We use the mode (maximum) as the line position:

$$\lambda_{\max} = \lambda_0 + \sigma\left(\frac{q - 1}{q}\right)^{1/q}. \quad (2)$$

The model we fit was the sum of two Weibull functions (one for Mg XII and one for Fe XXIII) with common q and σ parameters; the wavelength offset and the relative strengths of the lines were constrained to their theoretical differences, plus a constant continuum, over the 8.0–9.0 Å region. Given the best fit, we then determined confidence intervals via emcee, which also showed that q and σ were strongly correlated, with $q > 4$ ($\sigma > 0.1$), but with values as large as $q = 40$ acceptable (and corresponding $\sigma = 1.2$). The best fit has an asymmetric line, with a slightly more extended wing on the blue side. However, for the lowest acceptable values of $q \sim 4$, the profile is nearly Gaussian. The primary difference is that the peak is closer to the rest wavelength for the Weibull fit than for the Gaussian, which is probably offset to compensate for the slight asymmetry. Statistically, we cannot distinguish the difference, but the notion of some asymmetry agrees with expectations of more absorption at receding velocities. The lack of strong asymmetry is highly relevant to interpreting the dynamics. We show the fit and model profiles in Figure 6 and model parameters in Table 5.

An alternative approach meets that challenge and provides clear statistical support for the suggested asymmetry of the line profile. Following Pollock (2007), the HETG spectra at maximum light were fitted with an ensemble of lines with a single triangular velocity profile above an absorbed bremsstrahlung continuum. The ensemble of lines comprised 268 lines from 33 ionic species, each individual line strength considered a free parameter independent of the physical constraints of plasma-emission models except for fixing the 2:1 relative intensities of the H-like doublets. A comparison was made between symmetric and asymmetric models, the latter parameterized by blue, central, and red velocities showing where the profile reaches zero on either side of a central peak. The asymmetric model resulted in a C-Statistic improvement of $\Delta C = 55.7$ for the single extra degree of freedom over the constrained symmetric model, clear evidence of a departure from symmetry with best-fit velocities having the blue intercept of -2426 ± 103 km s^{-1}, the peak occurring at
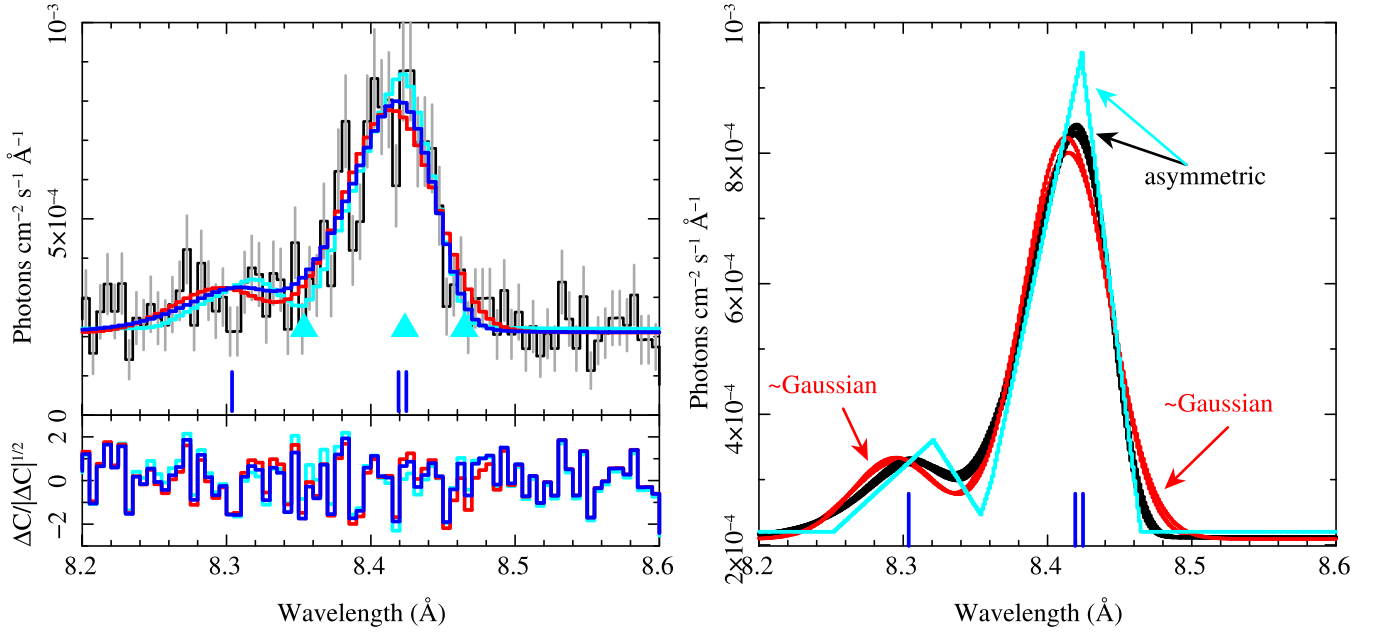
Figure 6. Left: the Mg XII region and fit with a Weibull distribution. The black histogram shows the data, the colored histograms show models, and the lower panel the respective residuals. The strong feature is the Mg XII doublet at 8.42 Å; the weak feature at 8.3 Å is an Fe XXIII line. The red model curve is for $q = 4$ (near Gaussian case), and blue is for $q = 42$ (acceptable solution). The blue residuals (lower panel) are slightly, but systematically, less than the red. Differences are very subtle, below statistical significance. The cyan curve shows the triangular profile model as fit to an ensemble of lines, and the cyan triangles indicate the parameters for blue, center, and red limits. Right: model profiles (unconvolved by the instrumental profile), all of them acceptable, for $q = 4$ (nearly Gaussian) and a Gaussian fit (red curves, labeled "∼Gaussian"), and for the Weibull fits with larger q (black, labeled "asymmetric"). These serve as a key to the model curves in the left panel. The long vertical tick-marks on the x-axes in each plot mark the line rest wavelengths for the Gaussian and Weibull fits.

Table 5
Weibull Fit Parameters for the Mg XII Region

Parameter	Value	stddev	Units
f(Mg XII)	4.60	0.55	10^{-5} photons cm^{-2} s^{-1}
λ_{max}	8.4198	0.002	Å
Δv	−43.7	79.7	km s^{-1}
σ	>0.1		
q	>4		
f(Fe XXIII)	0.70	0.19	10^{-5} photons cm^{-2} s^{-1}
f_c	20.03	0.55	10^{-5} photons cm^{-2} s^{-1} Å^{-1}

Note. "stddev" is the one standard deviation uncertainty. The Fe XXIII line shared the parameters σ and q, and was at a fixed wavelength offset from Mg XII of −0.1181 Å. The local continuum was parameterized by a constant level with flux f_c.

$+61 \pm 85$ km s^{-1}, and a red intercept of $+1525 \pm 80$ km s^{-1}. As shown in Figure 6, these ensemble velocities are entirely consistent with the morphology of the Weibull analysis of Mg XII reported above.

5.2. He-like Line Ratios

The He-like atomic structure has metastable levels that produce resonance (r), intercombination (i), and forbidden (f) lines in the soft X-ray band for several abundant elements, making them excellent diagnostics for temperature, density, and UV photo-excitation (Gabriel & Jordan 1969; Blumenthal et al. 1972). These have been used to estimate the radius of formation of X-rays in OB-star winds (Waldron & Cassinelli 2001; Leutenegger et al. 2006; Waldron & Cassinelli 2007). An intense UV field can depopulate the level of forbidden lines, since they are metastable, and the closer the emitting plasma is to the UV-strong

photosphere, the smaller the f/i flux ratio. High density in plasmas can produce the same effect (cf. Oskinova et al. 2017).

Since the X-ray flux of WR 25 comes predominantly from the shock cone, relatively far from the W-R and OB stars, we might not expect the f/i ratio for Ne, Mg, and Si (for which we have good resolution) to be affected, unless there is a significant diffuse UV field produced in the shocks themselves. We have used our plasma model as a baseline for investigating the f/i ratios in Ne IX, Mg XII, and Si XIII. Starting with this model, we introduce modified emissivities for the He-like lines using data produced from APEC (Foster et al. 2012).[8] To let the model adjust locally to each He-like region investigated, we allowed the normalization, Doppler shift, line widths, and elemental abundances to be free, as well as the f/i ratio parameter (we used density as a simple parameter to scale the ratio).

It is common to refer the ratio of the forbidden line flux to the intercombination line flux as $R = f/i$. The expected value without UV or collisional pumping is usually denoted as R_0. This quantity has a mild temperature dependence, with about a 10% increase with temperature where the line has significant emissivity. For R_0, we adopted the mean values as weighted by emission measure according to our adopted model of the emission measure distribution (see Section 4.1 and Table 3).

For Mg XI, we found that $R/R_0 > 0.3$ (90% confidence) or >0.4 (68% confidence). Ne IX, at the 90% confidence level, spans the entire range; at 68%, it has $R/R_0 > 0.25$. The best fit for Si XIII is consistent with the unexcited limit; the 90% and 68% lower limits to R/R_0, respectively, are 0.65 and 0.76. Upper limits for Ne, Mg, and Si were all 1.0, or in other words, they are consistent with no photoexcitation. The f line remains

---

[8] See https://space.mit.edu/cxc/analysis/he_modifier/index.html for data tables, a description, and an implementation for ISIS.

strong: that the f line is not depopulated led us to infer that the X-ray-emitting region is not located near enough to the individual stars in the binary to be significantly affected by their UV radiation. Similar findings are also seen in many colliding-wind binaries such as WR 147, WR 140, and WR 48a (Zhekov & Park 2010; Pollock et al. 2005; Zhekov et al. 2014), to name a few.

5.3. Variability

The Swift/XRT light curve indicates that the peak emission occurs around 10 days before periastron. The 0.3–1.5 keV XRT light curves exhibit a steep drop in the X-rays, indicating increased absorption that causes extinction of soft X-rays just after this peak and continues up to 10 days after periastron (Figure 2).

As seen in the schematic diagram of the WR 25 orbit in Figure 1 and the X-ray light curve in Figure 2, the on-axis HETG observations were carried out just around maximum light. The times of these two observations are indicated by green stars in Figure 2.

The off-axis HETG spectra, while of too low a resolution for determinations of line shape or width, do provide some spectral information. Further, the line fluxes and overall energy distribution provide some diagnostics of the plasma. By $\phi = 0.05$, the observed (absorbed) flux has dropped by about 40%, while the maximum temperature has risen from 50 to 85 MK. The absorbing column has also risen; our sightline passes through more of the W-R star's wind. The temperature increase is unexpected, since the stellar separations are about the same at the two phases, hence the wind–wind collision should be at the same relative velocity. At $\phi = 0.13$ when the collision is behind the W-R wind at a larger impact parameter from the W-R star than at $\phi = 0.05$ (see Figure 1) and there is less intervening matter along the line of sight, the absorption has dropped substantially as expected; the observed flux is about the same as at phase 0.05. Here, we might expect the somewhat higher temperature given that the winds are expected to collide at a somewhat higher relative velocity, but the fit actually shows a slightly lower value. At the higher maximum plasma temperature, we estimate a shock relative velocity of $\sim$2200 km s^{-1}.

The unabsorbed fluxes decrease steadily over the phase range from 0.95 to 0.13. We expect flux to generally scale inversely with the separation of the stars (see Table 2 for the separation relative to maximum separation). Since it does not strictly do this, it may indicate other than adiabatic processes, as suggested by Arora et al. (2019), who estimated that radiative processes become important near periastron.

During the two on-axis observations, ObsIDs 18616 and 19687, WR 25 was monitored optically with the Aspect Camera on board Chandra. The Aspect Camera is mounted parallel to the X-ray telescope boresight and read continuously during the observation approximately every 2.05 s. The Aspect Camera CCD has a spectral response from 4000 to 10000 Å so it is a redder wavelength range than Johnson UBV photometry. Flux calibration is based on a zero-magnitude star of G0 V spectral type. Conversion between V and B magnitudes and Aspect Camera magnitudes is available in Nichols et al. (2010). It has been shown that the Aspect Camera photometry is internally consistent to 1%–2%.

Figure 7 (top) shows the Aspect Camera (ACA) data for ObsIDs 18616 and 19687 plotted with WR 25 phase and the
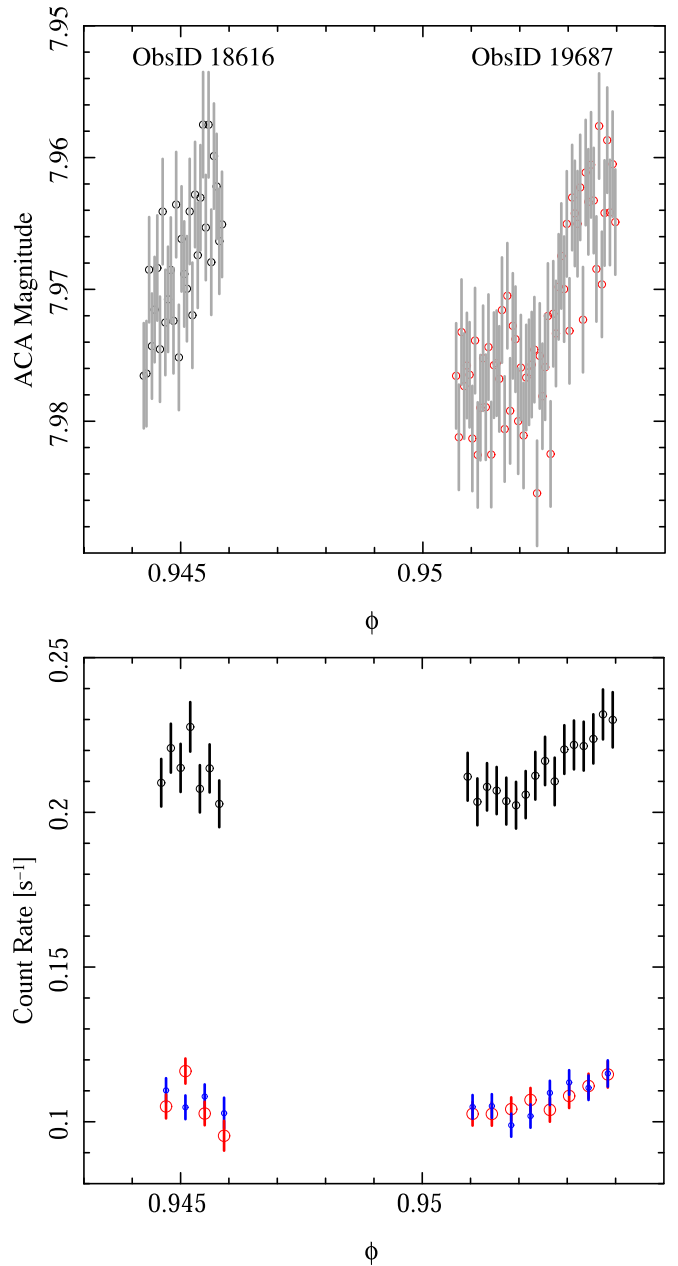
Figure 7. Top: the ACA magnitudes and estimated errors (see text) of WR 25 for ObsIDs 18616 and 19687. WR 25 was monitored with the optical ACA during these observations. The data are binned at 1 ks. The phase of the observations is shown on the x-axis. Bottom: the count-rate light curve for the on-axis pointings. The top shows the 1.7–17.0 Å band for a sum of count rates from HEG and MEG first orders. Below, the curves are shown for two bands, subdivided at 7.25 Å; small (blue) circles are the short-wavelength range, and larger circles (red) the long-wavelength range. There is no appreciable change in the hardness ratio for these two bands. Error bars are one standard deviation, and time bins were about 1 hr. The x-axis range spans about 2.5 days at about 10 days before periastron.

ACA magnitude. A 5% amplitude difference is seen in these light curves. Figure 7 (bottom) also shows the light curves of the dispersed X-ray photons for each ObsID, which only show an upward trend with time in the second ObsID. From the same plot, we see that the overall variability is about 15%, but since the trend does not show a constant rise with phase as the system approaches periastron, it could represent nonuniform density structure in the wind.

It is surprising to find that the ACA light curves for both ObsIDs show a similar rise in brightness (lower magnitude). We verified that no high background event took place during the acquisition of these data, and all guide stars were well tracked during the entire observation (E. Martin, private communication). To estimate the error in ACA magnitude, we used the mean of the standard deviations of the ACA magnitudes for two of the guide stars used in this observation, deriving a value of 0.004 ACA magnitude. The two guide stars selected were clearly constant in ACA magnitude, so the errors we show for the ACA magnitude of WR 25 are assumed to be the errors associated with a constant source. The ACA data are broadband, with no information on spectral distribution, so we cannot determine the cause of the change in magnitude during each observation. One possibility is a change in reddening, perhaps due to clumps of dust or density-enhanced gas clouds in the line of sight. WR 25 in fact lies in the line of sight to an enhanced thermal dust feature in Planck data. WR 25 has no intrinsic polarization (Fullard et al. 2020) but a large IPS angle (deviation of polarization angle with wavelength). Drissen et al. (1992) suggested that this deviation could be due to regions within the Carina Nebula that experience grain processing due to shock waves, and the large IPS angle determined for WR 25 (Fullard et al. 2020) supports this idea. However, intrinsic dust in the WR 25 system could also produce a dust absorption signature. Optical and IR monitoring would be required to study the time-dependent absorption in this line of sight.

6. Conclusions

We have presented the first high-resolution X-ray spectra of the colliding-wind binary WR 25, along with the context of long-term broadband X-ray monitoring with Swift. The pointed HETGS observations were near periastron, when the X-ray brightness is maximal. The colliding-wind shock region dominates the emission, being about an order of magnitude above that from stars of similar spectral type that lack wind–wind collisions.

Our primary results from fitting the high-resolution lines and the energy distribution, under the assumption that the emitting plasma is in collisional ionization equilibrium, are:

1. The pre-shock velocity is about $v \approx 1900 \, \mathrm{km \, s^{-1}}$;
2. Emission lines have a blueshifted centroid, which increases in magnitude with increasing wavelength, from about $-100 \, \mathrm{km \, s^{-1}}$ to about $-600 \, \mathrm{km \, s^{-1}}$ from Ar XVII to O XVIII. This is understood as likely due to the increased opacity of neutral matter, which increasingly absorbs emission from receding plasma.
3. Emission lines are resolved and broad, with an FWHM of about $2400 \, \mathrm{km \, s^{-1}}$, with no clear trend with wavelength. This is consistent with the velocities of the colliding stellar winds seen nearly along the line of sight in a shock cone. The constancy of the width with wavelength is somewhat at odds with the previous item, since increasing opacity with wavelength would hide receding material and narrow the lines. There might be significant turbulence in the shock cone that masks bulk flow effects.
4. The emission lines seem very nearly Gaussian, though formally, a slightly asymmetric profile is acceptable. The line shape depends critically on velocity fields and opacity. Hence, this should provide an important constraint for any detailed hydrodynamical models.

5. Within the pointed HETGS observations, the source X-ray flux was significantly variable, at a level of about 15%. While phase coverage was small, the X-ray changes seemed gray and non-secular with phase. They may represent clumpiness in the wind and not, for instance, changing absorption or temperature. The simultaneous optical photometry also showed variability, with about a 5% amplitude. One pointing showed a similar trend to the X-ray flux, which is intriguing, but the other observation did not show a correlation.

The off-axis HETGS spectra, while of higher resolution than the imaging mode, are blurred enough that the line centroid and profile cannot be meaningfully studied. The flux behavior does not show a simple dependence on stellar separation or phase, and may indicate that there nonadiabatic processes are significant near periastron. High-resolution spectra are required at these phases in order to determine the dynamics, and to provide crucial constraints on wind-shock models. For instance, at $\phi \sim 0.04$ (conjunction), we expect the shock-cone flow to be primarily away from us, so we would expect redshifted lines. The line width should also be smaller than near periastron since we are not viewing the cone transversely, but face-on. At the other conjunction (O star in front; $\phi \sim 0.8$, $-40 \, \mathrm{days}$), the shock cone would be concave toward the viewer, and we would expect blueshifted lines.

WR 25 is perhaps the best system for studying colliding-wind physics. It is bright, has a period amenable to phase-resolved studies in a relatively short time span, and most importantly, it appears to stay relatively transparent to the O4 star even when looking through the WN6 star's wind. Other systems, such as WR 140 ($P \sim 8 \, \mathrm{yr}$) or η Car ($P \sim 5 \, \mathrm{yr}$), are quite opaque during conjunction and do not allow the shock cone to be seen at soft X-ray energies. Blueshifted lines have regularly been observed in colliding-wind binaries, notably in WR 140, but redshifts only in θ Muscae, a complex multiple system where orbital dynamics seem to play no role. In WR 140, absorption by the WC-star wind at conjunction is far too strong for measurements to be feasible. The very massive WN systems Mk 34 and WR 21a both show deep extended minima at their relevant conjunction phases. While these are all interesting and relevant systems, WR 25 remains the best for studies of shock-cone dynamics about the whole orbit, and hence an excellent subject for the study of stellar winds.

This study can only be considered as the initial investigation into the dynamics, since more phase coverage is needed. But we have shown that such a study is feasible and would likely be fruitful with the Chandra/HETGS .

Appendix
Line Emission Fits with HETG

The detailed plots for the Gaussian fits for two on-axis observations (ObsIDs 18616 and 19687) with Chandra/HETGS are shown in Figures A.1–A.4.
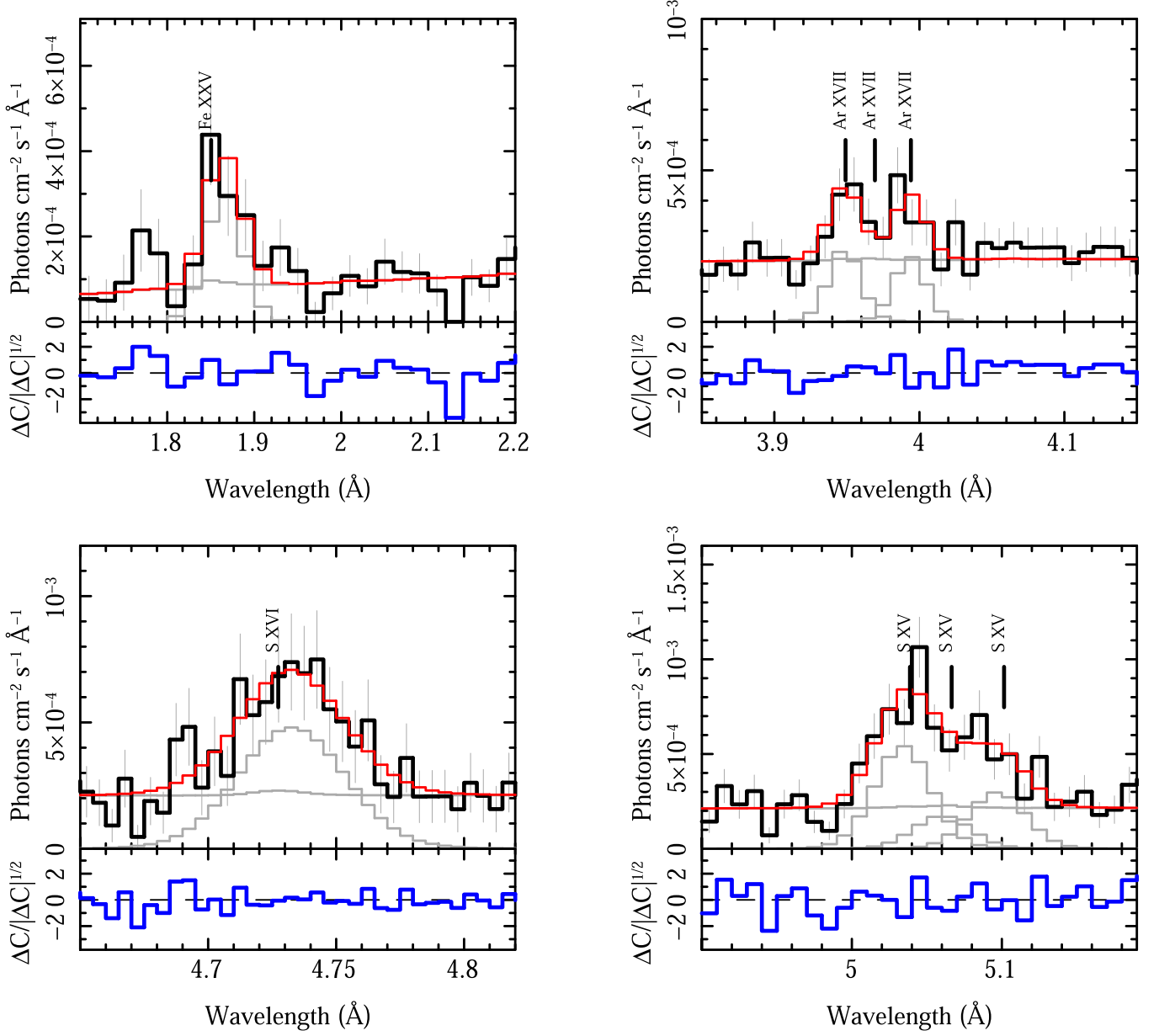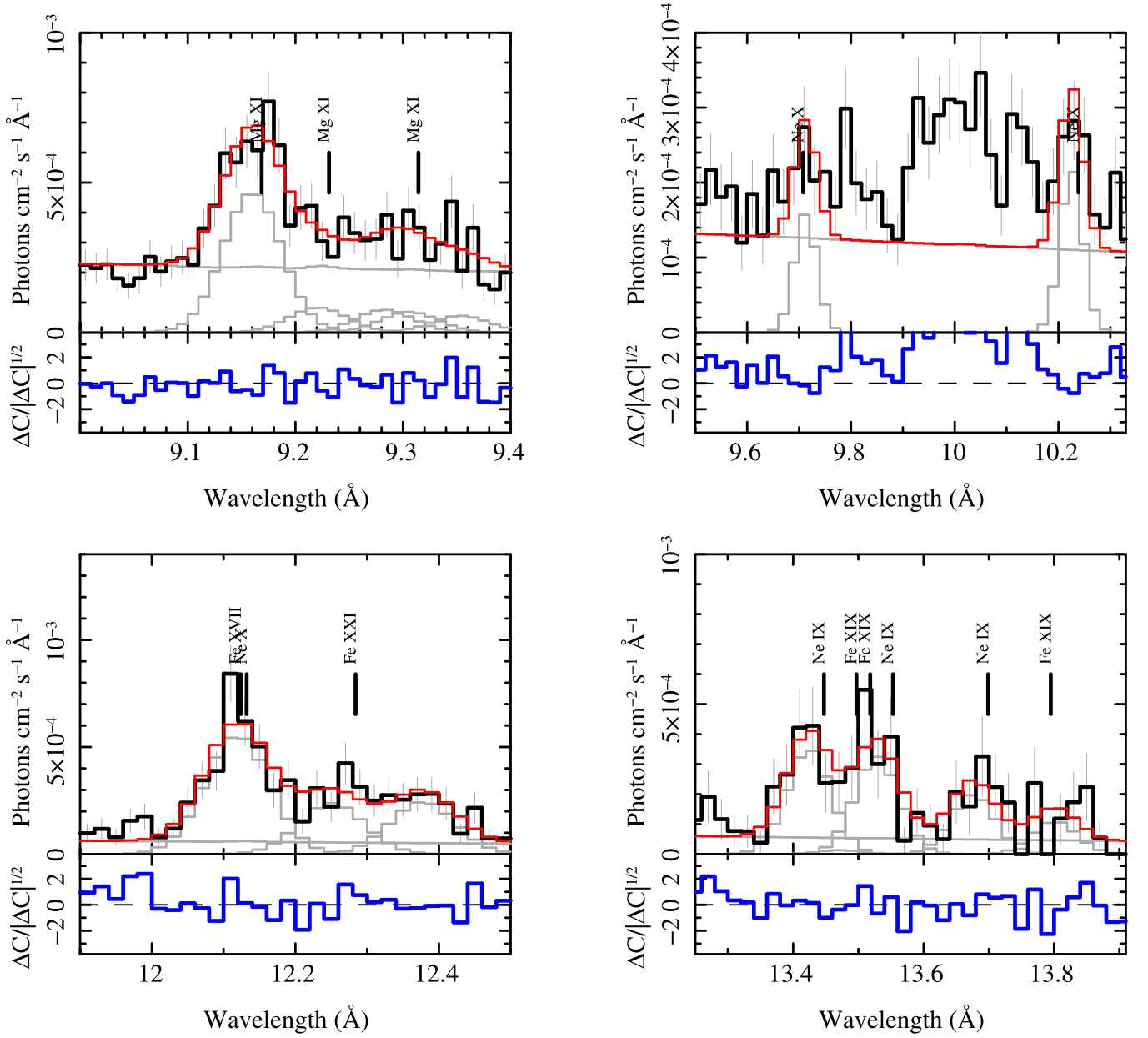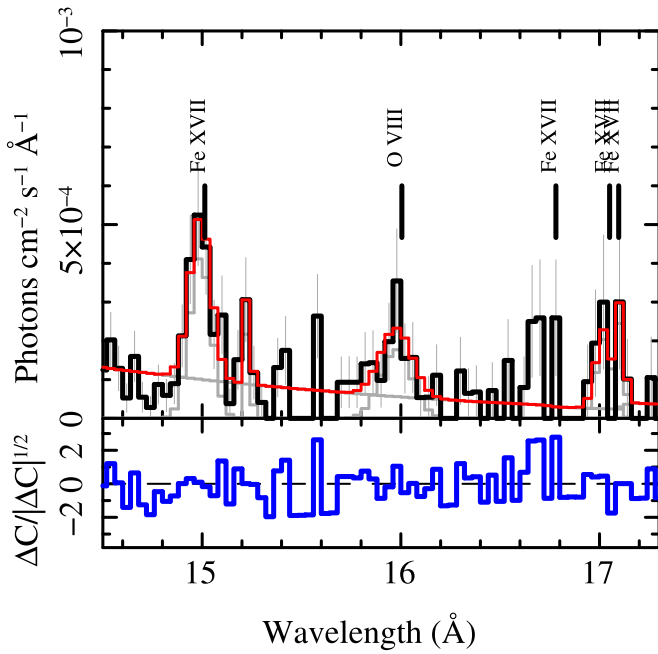

Figure A.1. Gaussian fits to several emission line regions for the on-axis observations. In each panel, the black histogram shows the flux spectrum for the combined HETG first orders, the red is the model, the gray are the individual components of the model, and the blue are the residuals.
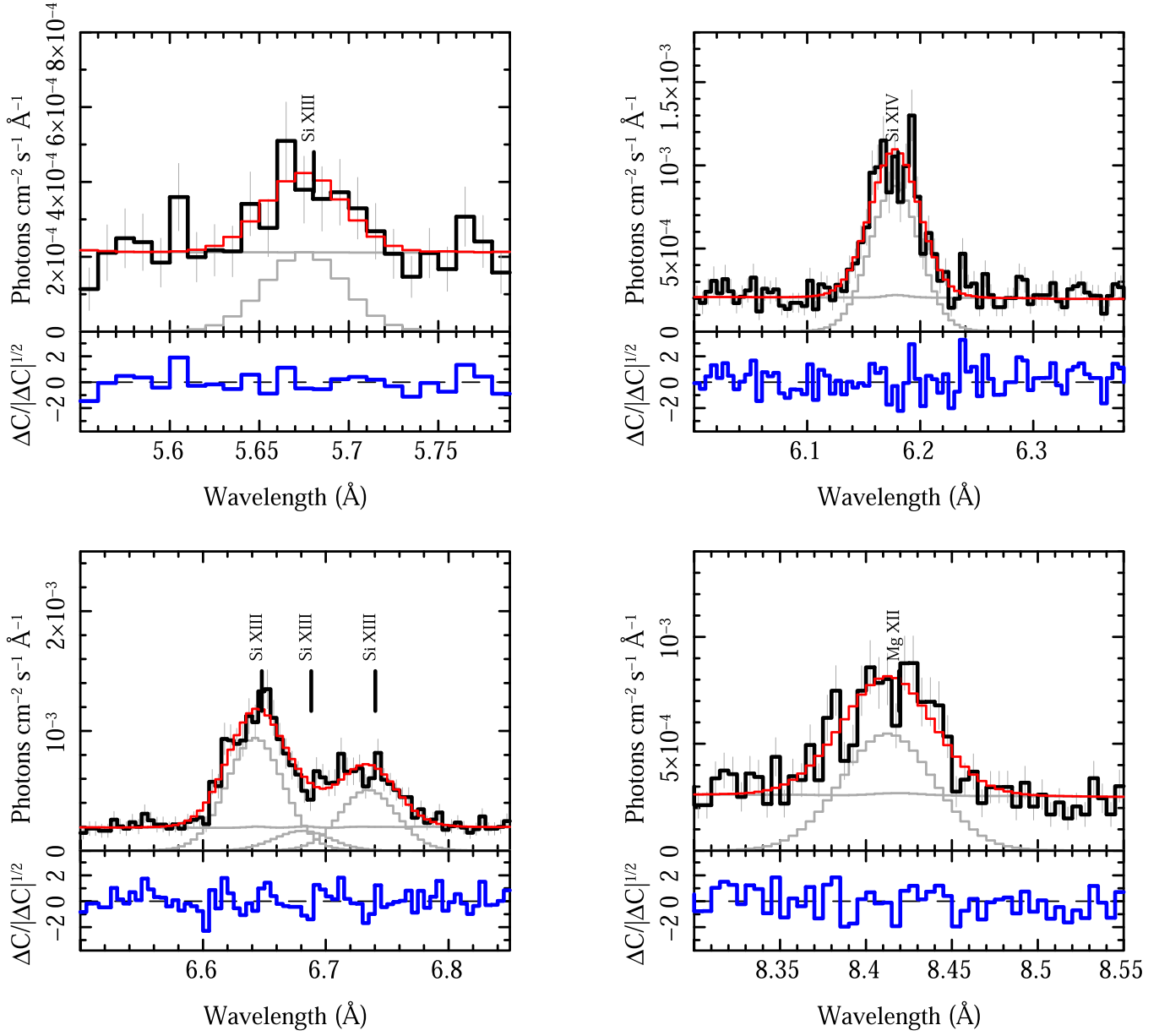
Figure A.2. Gaussian fits to several emission line regions for the on-axis observations. In each panel, the black histogram shows the flux spectrum for the combined HETG first orders, the red is the model, the gray are the individual components of the model, and the blue are the residuals.

Figure A.3. Gaussian fits to several emission line regions for the on-axis observations. In each panel, the black histogram shows the flux spectrum for the combined HETG first orders, the red is the model, the gray are the individual components of the model, and the blue are the residuals. Note that for the Ne x region at 9.5–10.3 Å, we have ignored the Fe-line complex and therefore the bump is visible between 9.8 and 10.1 Å.

Figure A.4. Gaussian fits to several emission line regions for the on-axis observations. In each panel, the black histogram shows the flux spectrum for the combined HETG first orders, the red is the model, the gray are the individual components of the model, and the blue are the residuals.

ORCID iDs

Pragati Pradhan https://orcid.org/0000-0002-1131-3059
David P. Huenemoerder https://orcid.org/0000-0002-3860-6230
Richard Ignace https://orcid.org/0000-0002-7204-5502
A. M. T. Pollock https://orcid.org/0000-0002-6737-538X
Joy S. Nichols https://orcid.org/0000-0003-3298-7455

References

Arnaud, K. A. 1996, in ASP Conf. Ser. 101, Astronomical Data Analysis Software and Systems V, ed. G. H. Jacoby & J. Barnes (San Francisco, CA: ASP), 17
Arora, B., Pandey, J. C., & De Becker, M. 2019, MNRAS, 487, 2624
Asplund, M., Grevesse, N., Sauval, A. J., & Scott, P. 2009, ARA&A, 47, 481
Blumenthal, G. R., Drake, G. W. F., & Tucker, W. H. 1972, ApJ, 172, 205
Cantó, J., Raga, A. C., & Wilkin, F. P. 1996, ApJ, 469, 729
Cassinelli, J. P., Ignace, R., Waldron, W. L., et al. 2008, ApJ, 683, 1052
Castor, J. I., Abbott, D. C., & Klein, R. I. 1975, ApJ, 195, 157
Corcoran, M. F., Liburd, J., Morris, D., et al. 2017, ApJ, 838, 45
Corcoran, M. F., Swank, J. H., Petre, R., et al. 2001, ApJ, 562, 1031
Crowther, P. A. 2007, ARA&A, 45, 177
Crowther, P. A., & Walborn, N. R. 2011, MNRAS, 416, 1311
Driessen, F. A., Sundqvist, J. O., & Kee, N. D. 2019, A&A, 631, A172
Drissen, L., Robert, C., & Moffat, A. F. J. 1992, ApJ, 386, 288
Feldmeier, A., Puls, J., & Pauldrach, A. W. A. 1997, A&A, 322, 878
Foreman-Mackey, D., Hogg, D. W., Lang, D., & Goodman, J. 2013, PASP, 125, 306
Foster, A. R., Ji, L., Smith, R. K., & Brickhouse, N. S. 2012, ApJ, 756, 128
Fruscione, A., McDowell, J. C., Allen, G. E., et al. 2006, Proc. SPIE, 6270, 62701V
Fullard, A. G., St-Louis, N., Moffat, A. F. J., et al. 2020, AJ, 159, 214
Gabriel, A. H., & Jordan, C. 1969, MNRAS, 145, 241
Gamen, R., Gosset, E., Morrell, N., et al. 2006, A&A, 460, 777
Gamen, R., Gosset, E., Morrell, N. I., et al. 2008, in Revista Mexicana de Astronomia y Astrofisica Conf. Ser. 33, Massive Stars: Fundamental Parameters and Circumstellar Interactions, ed. P. Bengalia, G. Bosch, & C. Cappa (Mexico: Instituto de Astronomía, UNAM), 91

Gayley, K. G. 2009, ApJ, 703, 89
Gayley, K. G., Owocki, S. P., & Cranmer, S. R. 1997, ApJ, 475, 786
Grant, D., Blundell, K., & Matthews, J. 2020, MNRAS, 494, 17
Hamaguchi, K., Corcoran, M. F., Gull, T. R., et al. 2016, ApJ, 817, 23
Hamann, W. R., Gräfener, G., Liermann, A., et al. 2019, A&A, 625, A57
Henley, D. B., Stevens, I. R., & Pittard, J. M. 2003, MNRAS, 346, 773
Hervé, A., Rauw, G., & Nazé, Y. 2013, A&A, 551, A83
Houck, J. C., & Denicola, L. A. 2000, in ASP Conf. Ser. 216, Astronomical Data Analysis Software and Systems IX, ed. N. Manset, C. Veillet, & D. Crabtree (San Francisco, CA: ASP), 591
Howarth, I. D., & van Leeuwen, F. 2019, MNRAS, 484, 5350
Huenemoerder, D. P., Gayley, K. G., Hamann, W. R., et al. 2015, ApJ, 815, 29
Huenemoerder, D. P., Ignace, R., Miller, N. A., et al. 2020, ApJ, 893, 52
Huenemoerder, D. P., Mitschang, A., Dewey, D., et al. 2011, AJ, 141, 129
Ignace, R. 2001, ApJL, 549, L119
Ignace, R. 2016, AdSpR, 58, 694
Ignace, R., Oskinova, L. M., & Foullon, C. 2000, MNRAS, 318, 214
Ignace, R., Waldron, W. L., Cassinelli, J. P., & Burke, A. E. 2012, ApJ, 750, 40
Kahn, S. M., Leutenegger, M. A., Cottam, J., et al. 2001, A&A, 365, L312
Krtička, J., Feldmeier, A., Oskinova, L. M., Kubát, J., & Hamann, W. R. 2009, A&A, 508, 841
Langer, N. 2012, ARA&A, 50, 107
Leutenegger, M. A., Paerels, F. B. S., Kahn, S. M., & Cohen, D. H. 2006, ApJ, 650, 1096
Lucy, L. B., & White, R. L. 1980, ApJ, 241, 300
Luo, D., McCray, R., & Mac Low, M.-M. 1990, ApJ, 362, 267
Muijres, L. E., de Koter, A., Vink, J. S., et al. 2011, A&A, 526, A32
Nazé, Y., Flores, C. A., & Rauw, G. 2012, A&A, 538, A22
Nichols, J. S., Henden, A. A., Huenemoerder, D. P., et al. 2010, ApJS, 188, 473
Oskinova, L. M., Huenemoerder, D. P., Hamann, W. R., et al. 2017, ApJ, 845, 39
Owocki, S. P., & Cohen, D. H. 2001, ApJ, 559, 1108
Owocki, S. P., Sundqvist, J. O., Cohen, D. H., & Gayley, K. G. 2013, MNRAS, 429, 3379
Pandey, J. C., Pandey, S. B., & Karmakar, S. 2014, ApJ, 788, 84
Parkin, E. R., & Gosset, E. 2011, A&A, 530, A119
Pittard, J. M. 2007, ApJL, 660, L141
Pittard, J. M., & Corcoran, M. F. 2002, A&A, 383, 636
Pittard, J. M., & Dawson, B. 2018, MNRAS, 477, 5640
Pittard, J. M., & Parkin, E. R. 2010, MNRAS, 403, 1657
Pollock, A. M. T. 1987, ApJ, 320, 283
Pollock, A. M. T. 2007, A&A, 463, 1111
Pollock, A. M. T. 2012, in ASP Conf. Ser. 465, Proc. of a Scientific Meeting in Honor of Anthony F. J. Moffat, ed. L. Drissen et al. (San Francisco, CA: ASP), 308
Pollock, A. M. T., & Corcoran, M. F. 2006, A&A, 445, 1093
Pollock, A. M. T., Corcoran, M. F., Stevens, I. R., & Williams, P. M. 2005, ApJ, 629, 482
Pollock, A. M. T., Crowther, P. A., Tehrani, K., Broos, P. S., & Townsley, L. K. 2018, MNRAS, 474, 3228
Prilutskii, O. F., & Usov, V. V. 1976, AZh, 53, 6
Puls, J., Vink, J. S., & Najarro, F. 2008, A&ARv, 16, 209
Rate, G., & Crowther, P. A. 2020, MNRAS, 493, 1512
Rauw, G., De Becker, M., Nazé, Y., et al. 2004, A&A, 420, L9
Rauw, G., Mahy, L., Nazé, Y., et al. 2014, A&A, 566, A107
Rauw, G., & Nazé, Y. 2016, AdSpR, 58, 761
Sander, A. A. C., Hamann, W. R., Todt, H., Hainich, R., & Shenar, T. 2017, A&A, 603, A86
Schild, H., Güdel, M., Mewe, R., et al. 2004, A&A, 422, 177
Schnurr, O., Casoli, J., Chené, A. N., Moffat, A. F. J., & St-Louis, N. 2008, MNRAS, 389, L38
Schulz, N. S., Chakrabarty, D., & Marshall, H. L. 2019, arXiv:1911.11684
Schweickhardt, J., Schmutz, W., Stahl, O., Szeifert, T., & Wolf, B. 1999, A&A, 347, 127
Seward, F. D., Forman, W. R., Giacconi, R., et al. 1979, ApJL, 234, L55
Skinner, S. L., Güdel, M., Schmutz, W., & Stevens, I. R. 2001, ApJL, 558, L113
Smith, N. 2014, ARA&A, 52, 487
Smith, R. K., Brickhouse, N. S., Liedahl, D. A., & Raymond, J. C. 2001, ApJL, 556, L91
Sota, A., Apellániz, J. M., Morrell, N. I., et al. 2014, ApJS, 211, 10
Stevens, I. R., Blondin, J. M., & Pollock, A. M. T. 1992, ApJ, 386, 265

Sugawara, Y., Tsuboi, Y., & Maeda, Y. 2008, A&A, 490, 259
Sundqvist, J. O., Owocki, S. P., Cohen, D. H., Leutenegger, M. A., & Townsend, R. H. D. 2012, MNRAS, 420, 1553
Sundqvist, J. O., Owocki, S. P., & Puls, J. 2018, A&A, 611, A17
Tehrani, K. A., Crowther, P. A., Bestenlehner, J. M., et al. 2019, MNRAS, 484, 2692
Tramper, F., Sana, H., Fitzsimons, N. E., et al. 2016, MNRAS, 455, 1275
Usov, V. V. 1992, ApJ, 389, 635

Walborn, N. R., Nichols, J. S., & Waldron, W. L. 2009, ApJ, 703, 633
Waldron, W. L., & Cassinelli, J. P. 2001, ApJL, 548, L45
Waldron, W. L., & Cassinelli, J. P. 2007, ApJ, 668, 456
Williams, P. M., van der Hucht, K. A., Pollock, A. M. T., et al. 1990, MNRAS, 243, 662
Zhekov, S. A. 2021, MNRAS, 500, 4837
Zhekov, S. A., Gagné, M., & Skinner, S. L. 2014, ApJ, 785, 8
Zhekov, S. A., & Park, S. 2010, ApJ, 721, 518